Unified view of low- and high-frequency regimes of atomic ionization in intense laser fields

Haruhide Miyagi and Kiyohiko Someda
Department of Basic Science, Graduate School of Arts and Sciences, The University of Tokyo, Komaba, Meguro-ku, Tokyo 153-8902, Japan

(Received 3 July 2009; published 21 August 2009)

On the basis of the Floquet formalism, a two-dimensional model atom in circularly polarized intense laser fields is analyzed. By solving the close-coupling equations, the pole positions of the scattering matrix are calculated on the complex quasienergy Riemann surface, and the pole trajectories with respect to the variation in the laser intensity are obtained for different laser frequency regimes. The behaviors of the pole trajectories indicate that the tunneling ionization is typically observed in the low-frequency regime, while the stabilization of the atom occurs in the high-frequency regime. The mechanisms of the atomic ionization in these two regimes are discussed from a unified point of view. The transition between the different frequency regimes can be explained by the change in the avoided crossings among the adiabatic potential curves for the radial motion of the electron.

DOI: 10.1103/PhysRevA.80.023416 PACS number(s): 32.80.Rm, 42.50.Hz, 32.80.Fb

I. INTRODUCTION

Recent advances in the technology of high power lasers have opened a new aspect of atomic and molecular physics. Atoms and molecules in intense laser fields have been found to exhibit various phenomena, such as molecular alignment and orientation, Coulomb explosion, above threshold ionization, high-harmonics generation, and so on [1]. Among a variety of phenomena attracting attentions of researchers, ionization is particularly significant because it is involved in many cases as a basic process or otherwise needed to be taken into account as a competing process of the phenomena under consideration.

Studies on ionization in intense laser fields already have a long history since the work of Keldysh [2]. When the laser frequency is sufficiently lower than the typical frequency of electron motions bound in an atom (or molecule), the ionization probability is well described by tunneling of an electron through the barrier of the instantaneous electrostatic potential energy. Theories along this line have extensively been developed. Among them, the Keldysh-Faisal-Reiss (KFR) theory [2–4] and the Ammosov-Delone-Krainov (ADK) theory [5] are widely accepted as the standard theory to describe the tunneling ionization in the low-frequency regime.

On the other hand, many theoretical studies indicate that high-frequency intense lasers can give rise to several intriguing phenomena, such as stabilization [6] and light induced state (LIS) [7,8]. The stabilization means the phenomenon in which the ionization rate decreases with increasing laser intensity in a certain range of intensity.

The stabilization phenomenon was first predicted by the theoretical study [6] based on the Floquet formalism, in which atoms in stationary intense fields are treated. Later on, particularly many studies have been reported the stabilization in one-dimensional (1D) models, for example, 1D Coulomb potential [9], 1D Gaussian potential [7,10–12], 1D Pöschl-Teller potential [13], and 1D square well potential [14,15]. On the other hand, the stabilization phenomena have also been found for three-dimensional (3D) systems, for example, an H atom in linearly and circularly polarized laser fields [16–20] and an H^- ion in linearly polarized laser fields [21]. The existence of the stabilization phenomenon was shown experimentally for the circular Rydberg state of a Ne atom in a linearly polarized laser field [22].

In contrast to the low-frequency regime, the motion of the atomic electrons for the high-frequency regime is reasonably considered to be dominated by Kramers-Henneberger (KH) potential, i.e., the time averaged potential in the acceleration gauge. Gavrila studied the stabilization phenomenon along this line and defined "quasistationary (adiabatic) stabilization" (QS) as the stabilization that appears in the framework of the Floquet formalism [23]. Popov *et al.* named the same phenomenon "KH stabilization" according to its mechanism [24]. Dörr and Potvliege discussed the mechanism of QS on the basis of the Keldysh parameter [25]. These studies have proposed slightly different mechanisms independently, and there exists no unified understanding of the mechanism of stabilization. On the other hand, no stabilization has been observed in the low-frequency regime.

In the studies reported so far, the low- and high-frequency regimes are separately discussed on the basis of the approximation verifiable only within each regime. The present study aims at discussing a unified picture which explains how the stabilization occurs in the high-frequency regime, why the stabilization does not occur in the low-frequency regime, and what governs the transition between two regimes. In this paper, a two-dimensional (2D) model mimicking an atom in circularly polarized laser field is analyzed. On the basis of the Floquet formalism, the close-coupling equations in the acceleration gauge are derived. By numerically solving these equations under the Siegert boundary condition, the pole positions of the scattering matrix (S matrix) on the complex quasienergy Riemann surface are calculated. The intensity dependence of the pole position was found to exhibit the stabilization in the high-frequency regime and the tunneling ionization in the low-frequency regime. An attention is focused on the effective potential matrix in the close-coupling equations for the radial wave functions. The adiabatic potentials obtained by diagonalizing that matrix were found to be useful in understanding the transition between the tunneling ionization in low-frequency regime and the stabilization in

the high-frequency regime. It is emphasized that the centrifugal potential of the 2D system plays an important role in clarifying the mechanism of the transition between two different regimes. Similar discussion is not possible if the 1D models are employed.

The paper is organized as follows. The 2D model is introduced in Sec. II A, and the close-coupling equations are derived in Sec. II B. In Sec. II C, the method of calculating the S-matrix pole trajectories is described, and the effective potential matrix is defined. The results of the calculation of the S-matrix pole trajectories are shown for several laser frequencies in Sec. III. The mechanisms of the atomic ionization in the low- and high-frequency regimes are discussed on the basis of the effective potential matrix in Sec. IV. Physical implications of the numerical results are discussed in Sec. V. The conclusion is given in Sec. VI.

II. MODEL AND FORMULATION

A. Model system

A 2D model mimicking an atom is considered. An electron is trapped in a 2D potential well interacting with a circularly polarized laser field. The time-dependent Schrödinger equation (TDSE) in the acceleration gauge (the KH frame) is expressed as (e.g., see [26])

$$i\frac{\partial}{\partial t}\Psi(\boldsymbol{r},t)=\left(-\frac{1}{2}\Delta_2+V(\boldsymbol{r}+\boldsymbol{\alpha}(t))\right)\Psi(\boldsymbol{r},t), \tag{1}$$

where Δ_2 is the 2D Laplacian operator. The atomic units are used throughout this paper. The potential function $V(\boldsymbol{r})$ represents a 2D isotropic potential well expressed by a Gaussian function,

$$V(\boldsymbol{r})=-V_0\exp[-(r/r_0)^2], \tag{2}$$

with $V_0=r_0=1.404$. This potential well supports only one bound state at the energy $E=-0.477$. The vector $\boldsymbol{\alpha}(t)$ is related to the vector potential $\boldsymbol{A}(t)$,

$$\boldsymbol{A}(t)=\frac{A}{\sqrt{2}}(\hat{\boldsymbol{x}}\cos\omega t-\hat{\boldsymbol{y}}\sin\omega t), \tag{3}$$

and defined as

$$\boldsymbol{\alpha}(t)=\int^t\boldsymbol{A}(t')dt'=\frac{\alpha}{\sqrt{2}}(\hat{\boldsymbol{x}}\sin\omega t+\hat{\boldsymbol{y}}\cos\omega t), \tag{4}$$

where $\hat{\boldsymbol{x}}$ and $\hat{\boldsymbol{y}}$ are the unit vectors along the x and y axes, respectively, A represents the magnitude of the vector potential, ω is the angular frequency of the laser field, and $\alpha=A/\omega$ is the ponderomotive radius which represents the excursion amplitude of the classical quiver motion of an electron in the laser field.

For the comparison with the 2D model, a 1D model is considered. An electron is trapped in a 1D potential well interacting with a linearly polarized laser field. The 1D potential function $V_{1D}(x)$ is defined as a Gaussian function,

$$V_{1D}(x)=-\exp(-x^2). \tag{5}$$

This 1D potential well supports only one bound state at the energy $E=-0.477$. The values of the parameters of the 2D Gaussian potential function, $V_0=r_0=1.404$, were so determined that the energy of the bound state coincides with that of the 1D model. The TDSE in the acceleration gauge for the 1D model is given in Ref. [12]. The definitions of the ponderomotive radius α and the magnitude of the vector potential A for the 1D model are the same with those for the 2D model. In these definitions, the laser intensity, i.e., the energy flux density of the laser field, is the same for both the models when the values of α are the same.

B. Derivation of the close-coupling equations

According to the Floquet theorem, the solutions of the TDSE [Eq. (1)] can be expressed as

$$\Psi(\boldsymbol{r},t)=e^{-iEt}\sum_{n=-\infty}^{\infty}\Phi_n(\boldsymbol{r})e^{in\omega t}, \tag{6}$$

where E is the quasienergy [27]. On the other hand, the potential function in the TDSE [Eq. (1)] can be written in an explicit form by using Eqs. (2) and (4) and eventually expanded in the Fourier series as follows:

$$\begin{aligned}V[\boldsymbol{r}+\boldsymbol{\alpha}(t)]&=-V_0\exp\left\{-\frac{1}{r_0^2}\left[\left(x+\frac{\alpha}{\sqrt{2}}\sin\omega t\right)^2+\left(y+\frac{\alpha}{\sqrt{2}}\cos\omega t\right)^2\right]\right\}\\&=-V_0\exp\left(-\frac{r^2}{r_0^2}-\frac{\alpha^2}{2r_0^2}\right)\exp\left(-\frac{\sqrt{2}\alpha r}{r_0^2}\sin(\omega t+\phi)\right)\\&=\sum_{n=-\infty}^{\infty}V_n(r;\alpha)e^{in(\omega t+\phi)},\end{aligned} \tag{7}$$

where ϕ is the azimuthal angle of the electron coordinate and the expansion coefficient $V_n(r;\alpha)$ is given by

$$V_n(r;\alpha)=-V_0\exp\left(-\frac{r^2}{r_0^2}-\frac{\alpha^2}{2r_0^2}\right)i^nI_n\left(\frac{\sqrt{2}\alpha r}{r_0^2}\right). \tag{8}$$

Here, $I_n(\cdot)$ is the nth order modified Bessel function of the first kind. By substituting Eqs. (6) and (7) into the TDSE [Eq. (1)], one obtains coupled equations,

$$\begin{aligned}&\left(-\frac{1}{2}\Delta_2+n\omega\right)\Phi_n(\boldsymbol{r})+\sum_{m=-\infty}^{\infty}V_{n-m}(r;\alpha)e^{i(n-m)\phi}\Phi_m(\boldsymbol{r})\\&\quad=E\Phi_n(\boldsymbol{r}).\end{aligned} \tag{9}$$

Each Floquet component $\Phi_n(\boldsymbol{r})$ is expanded in the 2D partial waves as

$$\Phi_n(\boldsymbol{r})=\sum_{M=-\infty}^{\infty}f_n^M(r)e^{iM\phi}, \tag{10}$$

where M is the angular momentum quantum number and $f_n^M(r)$ is the radial wave function. Substituting Eq. (10) into Eq. (9), one obtains the close-coupling equations,

$$\left[-\frac{1}{2r}\frac{d}{dr}\left(r\frac{d}{dr}\right)+\frac{M^2}{2r^2}+n\omega\right]f_n^M(r)+\sum_{m=-\infty}^{\infty}V_{n-m}(r;\alpha)f_m^{M-n+m}(r)=Ef_n^M(r). \quad (11)$$

By introducing a new quantum number,

$$\mu = M - n, \quad (12)$$

and a new radial wave function $g_n^\mu(r)$,

$$g_n^\mu(r) = f_n^M(r), \quad (13)$$

Eq. (11) is simplified in the form

$$\left[-\frac{1}{2r}\frac{d}{dr}\left(r\frac{d}{dr}\right)+\frac{(n+\mu)^2}{2r^2}+n\omega\right]g_n^\mu(r)+\sum_{m=-\infty}^{\infty}V_{n-m}(r;\alpha)g_m^\mu(r)=Eg_n^\mu(r). \quad (14)$$

The radial functions with a different Fourier index n are coupled with each other, while there is no coupling with respect to the index μ. The index μ is a good quantum number originating from the rotational symmetry of the system under consideration, and Eq. (14) can be solved for each μ separately. When μ is replaced by $\mu+1$ in Eq. (14), the equation can be kept invariant if n and E are replaced by $n-1$ and $E-\omega$, respectively. Hence, it suffices to solve the close-coupling equations [Eq. (14)] only for $\mu=0$. The quasienergy for $\mu\neq 0$ can be obtained simply by shifting the complex quasienergy by $\mu\omega$. This is the manifestation of the periodicity of the quasienergy spectrum in the Floquet formalism. By truncating the number of the Floquet channels so as to include N channels, the close-coupling equations [Eq. (14)] can be written in the matrix form,

$$-\frac{1}{2r}\frac{d}{dr}\left(r\frac{d}{dr}\right)\boldsymbol{g}^\mu(r)+\boldsymbol{V}_{\text{eff}}^\mu(r;\alpha)\boldsymbol{g}^\mu(r)=E\boldsymbol{g}^\mu(r), \quad (15)$$

where $\boldsymbol{g}^\mu(r)$ is a column vector with N components and $\boldsymbol{V}_{\text{eff}}^\mu(r;\alpha)$ is the $N\times N$ *effective potential matrix* defined by

$$(\boldsymbol{V}_{\text{eff}}^\mu(r;\alpha))_{nm}=\left(\frac{(n+\mu)^2}{2r^2}+n\omega\right)\delta_{nm}+V_{n-m}(r;\alpha). \quad (16)$$

C. Method of calculation of the *S*-matrix pole on the complex quasienergy Riemann surface

In the present formalism, the ionization of the atom originally in a bound state is described by the decay of a quasibound state. According to the scattering theory, the quasibound states correspond to the poles of the S matrix on the complex quasienergy Riemann surface. The pole positions of the S matrix can be determined by solving Eq. (14) under the Siegert boundary condition in the asymptotic region,

$$g_n^\mu(r)\overset{r\to\infty}{\to}\text{const}\times H_{n+\mu}^{(+)}(k_n r), \quad (17)$$

and the usual boundary condition at the origin,

$$g_n^\mu(r)\overset{r\to 0}{\to}\text{const}\times r^{|n+\mu|}. \quad (18)$$

In Eq. (17), $H_{n+\mu}^{(+)}(k_n r)$ is the Hankel function of the first kind, and it should be noted that this function is multivalued for the complex variable (see Appendix A). The symbol k_n is the momentum of the electron in the nth Floquet channel defined by

$$k_n = \pm\sqrt{2(E-n\omega)}. \quad (19)$$

The sign of k_n determines the Riemann sheet on which the pole is located. The sign + (−) corresponds to the physical (unphysical) sheet with respect to the nth Floquet channel. Therefore, a set of signs of k_n is needed to specify the Riemann sheet uniquely. According to Ref. [13], the symbol $\Sigma=(\ldots,\sigma_{n-1},\sigma_n,\sigma_{n+1},\ldots)$ is defined, where σ_n represents the sign of k_n given in Eq. (19).

The poles of the S matrix can be classified into two categories, dominant pole and shadow pole [28]. The dominant pole leads to the wave function with the physical asymptotic behavior, while the shadow pole leads to that with an unphysical boundary condition. A pole located in the region $n\omega<\text{Re}\,E<(n+1)\omega$ is a dominant pole when the combination of the signs is

$$\Sigma=(\ldots,\sigma_{n-1},\sigma_n,\sigma_{n+1},\sigma_{n+2},\ldots)=(\ldots,-,-,+,+,\ldots)\equiv\Sigma_n. \quad (20)$$

Otherwise, the pole is a shadow pole. Here, an abbreviation Σ_n is defined as the combination of signs for the dominant poles in the region $n\omega<\text{Re}\,E<(n+1)\omega$.

The positions of dominant and shadow poles on the complex quasienergy Riemann surface are calculated by solving the close-coupling equation in the matrix form [Eq. (15)] under the Siegert boundary condition [Eq. (17)] with the specified set of signs Σ. The detail of the numerical procedure is discussed in Appendix B. The dominant pole positions at several selected values of α were obtained by the preliminary calculation on the basis of the complex-scaling Floquet method [11,13] and were used for the initial guess of E needed in the procedure of solving the close-coupling equations. The S-matrix pole trajectories were calculated by gradually changing the value of α with fixed ω. The results shown in Sec. III were obtained from the calculation including the Floquet channels $n=-15,\ldots,15$, i.e., the total number of the Floquet channel is $N=31$.

III. *S*-MATRIX POLE TRAJECTORY

The calculation of the S-matrix pole trajectories was carried out for the case of $\mu=0$. The typical trajectories are shown in Fig. 1. The values of angular frequencies are $\omega=0.3$, 0.4, 0.5, and 0.6. For the cases of $\omega=0.5$ and 0.6 the energy of one photon exceeds the binding energy of 0.477 of the bound state, while for the other cases ionization requires multiphoton absorption. The values of $\omega=0.3$ and 0.6 are used to be representative values for the low- and high-frequency regimes, respectively.

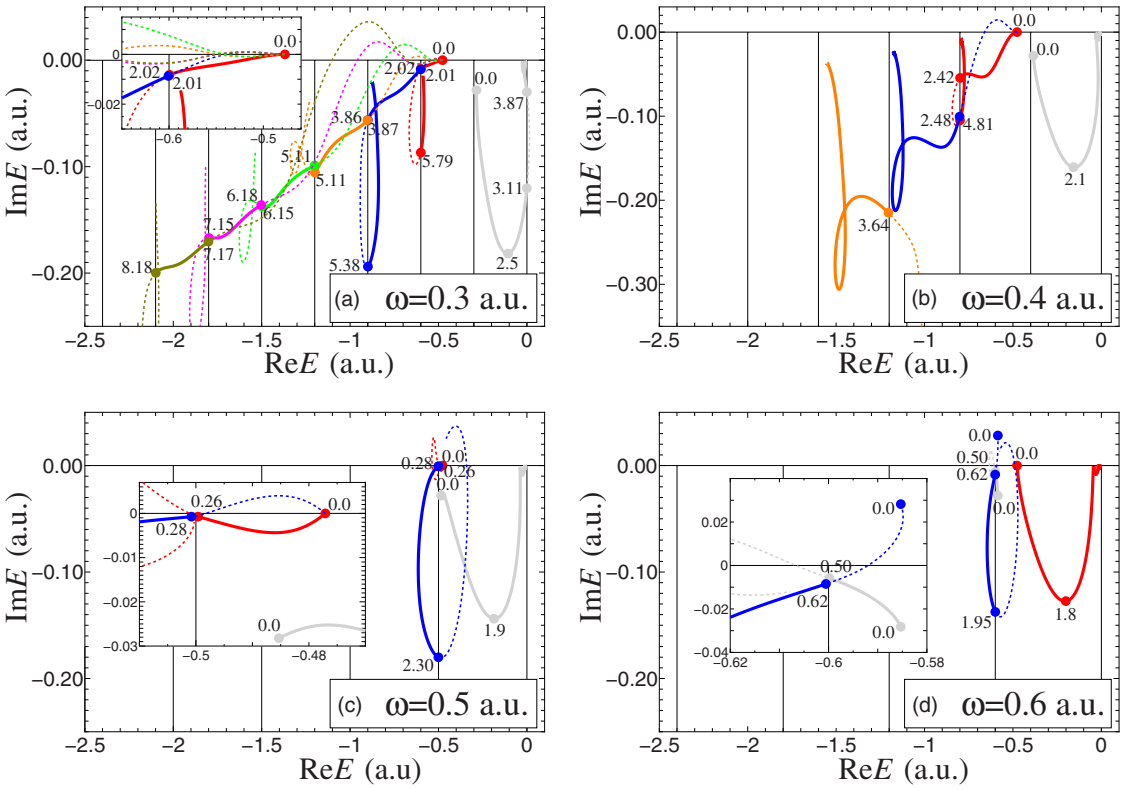

FIG. 1. (Color online) The S-matrix pole trajectories of the 2D model for four different laser angular frequencies: (a) $\omega=0.3$, (b) $\omega=0.4$, (c) $\omega=0.5$, and (d) $\omega=0.6$. The pole trajectories are indicated by solid curves when the poles are dominant poles and by dotted curves when they are shadow poles. The vertical lines represent the cuts originating from the branch points at the channel thresholds. The numerical values near the circles indicate the values of α at these points. The insets in panels (a), (c), and (d) are magnifications of a part of each figure. The trajectories originate, except several cases, from either the poles of the bound state at $E=-0.477$ or its shadow poles. The exceptions are as follows: the (gray) trajectories in panels (a)–(d) start from the point $E=0.0147-\omega-0.028\,23i$, which corresponds to the shape resonance on the $M=-1$ channel; the (orange) leftmost trajectory in panel (b) comes from an unknown point with $\mathrm{Im}\,E<-0.35$; and the (blue) trajectory in panel (d) starts from the point $E=-0.585+0.0282i$, which corresponds to one of the shadow poles of the complex conjugate pole of the shape resonance.

A. Low-frequency regime

The pole trajectories for the low-frequency regime ($\omega=0.3$) are shown in Fig. 1(a). With increasing laser intensity, the pole originating from the bound state leaves the real axis downward and becomes a dominant pole on the Σ_{-2} sheet. However, that pole crosses leftward the channel threshold $\mathrm{Re}\,E=-0.6$ at $\alpha=2.01$ and becomes a shadow pole. On the other hand, one of the shadow poles of the bound state also leaves the real axis downward on the Σ_{-3} sheet. This pole passes leftward the threshold $\mathrm{Re}\,E=-0.6$ at $\alpha=2.02$ and becomes a dominant pole. These threshold crossings of two poles described above take place at approximately the same value of α and at approximately the same point in the complex E plane, so that two poles seem to exchange their roles with each other at the channel threshold. The new dominant pole continues to travel leftward and passes the next threshold $\mathrm{Re}\,E=-0.9$ at $\alpha=3.87$, where it becomes a shadow pole again. At this threshold, the role of the dominant pole is taken by another pole, which has been traveling on the Σ_{-4} sheet. It should be noted that the third pole also originates from one of the shadow poles of the bound state. Similar exchanges are further repeated at the thresholds located at $\mathrm{Re}\,E=-1.2$, -1.5, and -1.8. As a result, pieces of the dominant pole trajectories are connected with each other so as to form one almost continuous trajectory.

The connected trajectory of dominant poles represents a resonance state of the atom, which adiabatically changes its property with laser intensity. The left-downward movement along the connected trajectory of the dominant poles means that the energy of that resonance state is broadened and shifted downward monotonically with increasing α. Such shift has been known as the ponderomotive energy shift [28]. The observed adiabatic change is predicted by the KFR theory [2–4] and interpretable as the tunneling ionization or the barrier-suppression ionization (BSI), which typically takes place in the low-frequency regime. It is remarkable that all the dominant poles appearing at each threshold correlate to the shadow poles of the bound state on each Riemann sheet. The member poles of the connected trajectory of the dominant poles become shadow poles again after they handed over their roles to the successors. The (red) pole on the Σ_{-2} sheet and the (blue) pole on the Σ_{-3} sheet, however, recross the channel threshold rightward and become dominant poles again. Such sudden emergence of a dominant pole has been known as the LIS [7,8]. Moreover, these two LIS poles move upward, i.e., in the direction of decreasing reso-

nance width, with increasing α. This is the stabilization phenomenon.

On the other hand, the trajectory starting from the point $E=-0.2853-0.028\ 23i$ on the Σ_{-1} sheet moves in the direction of increasing Re E, i.e., the direction opposite to the ponderomotive energy shift. As regard to Im E, that pole initially moves downward but begins to move upward at $\alpha=2.5$. This is also the stabilization phenomenon. The starting point $E=-0.2853-0.028\ 23i$ is the pole position of a shape resonance. The 2D Gaussian potential well possesses a doubly degenerate shape resonance at $E_{\mathrm{res}}=0.0147-0.028\ 23i$ with the angular momentum quantum number $M=\pm 1$. As a result, the pole of the shape resonance of $M=-1$ is located at $E=E_{\mathrm{res}}-\omega=-0.2853-0.028\ 23i$ in the present system.

B. Intermediate-frequency regime

The case of $\omega=0.4$ is shown in Fig. 1(b). Unlike the case of $\omega=0.3$, the continuous exchanges of dominant and shadow poles are not observed. The dominant pole originating from the bound state moves on the Σ_{-2} sheet. It passes leftward the threshold Re $E=-0.8$ at $\alpha=2.42$ and becomes a shadow pole. On the other hand, one of the shadow poles of the bound state moves on the Σ_{-3} sheet. It passes leftward the threshold Re $E=-0.8$ at $\alpha=2.48$ and becomes a dominant pole. These threshold crossings of two trajectories take place at roughly the same value of α and at roughly the same point in the complex E plane. However, the connection is far less smooth than in the case of $\omega=0.3$. The exchange of the roles of dominant and shadow poles is observed only at this threshold. No successive exchanges take place unlike the case of $\omega=0.3$. At $\alpha=4.81$, the shadow pole on the Σ_{-2} sheet passes rightward the threshold Re $E=-0.8$ and becomes a dominant pole again. In addition, another shadow pole comes from a certain unknown point in the region Im $E<-0.35$ and moves on the Σ_{-4} sheet. This pole becomes a dominant pole by passing leftward the threshold Re $E=-1.2$ at $\alpha=3.64$. On the other hand, the shape resonance pole at $E=E_{\mathrm{res}}-\omega=-0.3853-0.028\ 23i$ moves on the Σ_{-1} sheet and exhibits the stabilization. In summary, four dominant poles coexist for $\alpha\geq 4.81$. Two of them, i.e., one on the Σ_{-2} sheet and the other on the Σ_{-4} sheet, are the LISs. All the dominant poles show the stabilization phenomenon when the laser intensity becomes sufficiently large.

The case of $\omega=0.5$ is shown in Fig. 1(c). In this case, the energy of one photon slightly exceeds the binding energy of 0.477. The pole originating from the bound state moves leftward on the Σ_{-1} sheet and becomes a shadow pole at the threshold Re $E=-0.5$ when $\alpha=0.26$. A shadow pole of the bound state initially moves on the $(\ldots,\sigma_{-3},\sigma_{-2},\sigma_{-1},\sigma_0,\ldots)=(\ldots,+,+,-,+,\ldots)$ sheet. It crosses the real axis downward and enters the Σ_{-2} sheet. At $\alpha=0.28$, the pole becomes a dominant pole by passing leftward the threshold Re $E=-0.5$. These threshold crossings of two trajectories take place at approximately the same value of α and at approximately the same point in the complex E plane as in the case of $\omega=0.3$. The role of the first dominant pole seems to be succeeded by the second dominant pole. Unlike the case of $\omega=0.3$, however, the latter pole on the Σ_{-2} sheet does not continue to travel left downward. At $\alpha=2.30$, that pole passes rightward the threshold Re $E=-0.5$ and becomes a shadow pole again. The ponderomotive energy shift is not observed. On the other hand, the pole originating from the shape resonance at $E=E_{\mathrm{res}}-\omega=-0.4853-0.028\ 23i$ exhibits the stabilization phenomenon.

C. High-frequency regime

The trajectories in the high-frequency regime $\omega=0.6$ are shown in Fig. 1(c). The behaviors are totally different from the former cases. The pole originating from the bound state and that from the shape resonance behave conversely. The pole of the bound state begins to move right downward on the Σ_{-1} sheet and eventually exhibits the stabilization. On the other hand, the pole of the shape resonance at $E=E_{\mathrm{res}}-\omega=-0.5853-0.028\ 23i$ on the same sheet moves left upward and becomes a shadow pole by passing the threshold Re $E=-0.6$ at $\alpha=0.50$. In addition, a shadow pole starts from the point $E=-0.5853+0.028\ 23i$ on the $(\ldots,\sigma_{-3},\sigma_{-2},\sigma_{-1},\sigma_0,\ldots)=(\ldots,+,+,-,+,\ldots)$ sheet. The location of this point coincides with the complex conjugate point of the shape resonance pole. The pole of shape resonance at $E=E_{\mathrm{res}}-\omega$ on the Σ_{-1} sheet gives rise to the complex conjugate pole at $E=E_{\mathrm{res}}^{*}-\omega$. The observed shadow pole originates from a shadow pole of this complex conjugate pole. That shadow pole passes the real axis downward and enters the Σ_{-2} sheet. At $\alpha=0.62$, the pole becomes a dominant pole by passing leftward the threshold Re $E=-0.6$. This emergence of the dominant pole seems to be coincident with the disappearance of the dominant pole originating from the shape resonance. It could be interpreted as the succession of the role, as observed in the case of $\omega=0.3$, although the connection of two trajectories is not smooth.

The similar behaviors of pole trajectories have been observed in 1D models, i.e., 1D Gaussian potential [10–12], 1D Pöschl-Teller potential [13], and 1D square well potential [14,15]. In order to make a direct comparison with the 2D results calculation was carried out for the 1D Gaussian potential with directly comparable parameters given in Eq. (5). Figure 2 shows the pole trajectories of the 1D model with the laser frequency $\omega=0.6$. The dominant pole originating from the bound state exhibits the stabilization phenomenon. The shape of the trajectory resembles that of the 2D model. An LIS can be seen to emerge at the threshold Re $E=-0.6$, and this LIS pole behaves like the pole on the Σ_{-2} sheet of the 2D model. The origin of this LIS is one of the shadow poles of an antibound state (virtual state) [29] located at $E_{\mathrm{anti}}=-0.0305$, which is shifted to $E=E_{\mathrm{anti}}-\omega=-0.6305$ in the Floquet calculation.

IV. POTENTIAL CURVES FOR RADIAL MOTION AND MECHANISMS OF IONIZATION

As discussed so far, the tunneling ionization accompanied with the ponderomotive energy shift is typically observed in the low-frequency regime. In the high-frequency regime, however, the resonance state originating from the bound state exhibits the stabilization phenomenon instead of the pon-

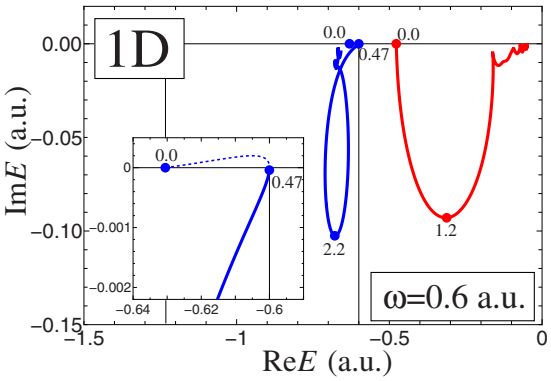

FIG. 2. (Color online) The S-matrix pole trajectories of the 1D model with $\omega=0.6$. The right (red) trajectory originates from the pole of the bound state at $E=-0.477$. The left (blue) trajectory originates from one of the shadow poles of the antibound state at $E=-0.0305-\omega=-0.6305$.

deromotive energy shift. In order to analyze the mechanisms of these phenomena and transition between two regimes, the attention is focused on the effective potential matrix in Eq. (16). The adiabatic potential curves for the radial motion are obtained by the eigenvalues of the effective potential matrix plotted as a function of r. On the other hand, the diagonal elements directly give the diabatic potential curves. The conventional KH potential in the high-frequency approximation corresponds to the diabatic potential $[V_{\mathrm{eff}}^{\mu=0}(r;\alpha)]_{00}$.

A. Low-frequency regime

Both the adiabatic and diabatic potential curves for the case $\omega=0.3$ are shown in Fig. 3. The adiabatic potential curves are obtained by diagonalization of the effective potential matrix [Eq. (16)] including the Floquet channels $n=-10,\ldots,10$. When $\alpha=0$, the adiabatic and the diabatic potential curves coincide with each other by definition. As can be seen in Fig. 3, the potential curve of $M=0$ exhibits a deep well of the Gaussian function in Eq. (2). With increasing M, the potential well becomes shallow due to the centrifugal force, and eventually the potential becomes purely repulsive. When α increases, the adiabatic potential curves begin to exhibit avoided crossings with each other. When $\alpha=1.0$, the lowest adiabatic curve comes to have a barrier, through which the tunneling ionization can take place. When $\alpha \geq 2.0$, the effects of the avoided crossings create a new potential well separated from the bunch of repulsive potential curves. The resonance originating from the bound state has changed into a kind of resonance formed inside or above the new potential well. As α increases, the potential well shifts downward along the envelope of the repulsive curves, and, in accordance with it, the resonance energy also shifts downward.

The formation of the new potential well is explicable by level repulsions among the diabatic curves. The r dependence of the off-diagonal elements of the effective potential matrix is shown in Fig. 4. The absolute value of the off-diagonal element, $|V_n(r;\alpha)|(n\neq 0)$, has a maximum. Around this maximum, the level repulsions among the diabatic

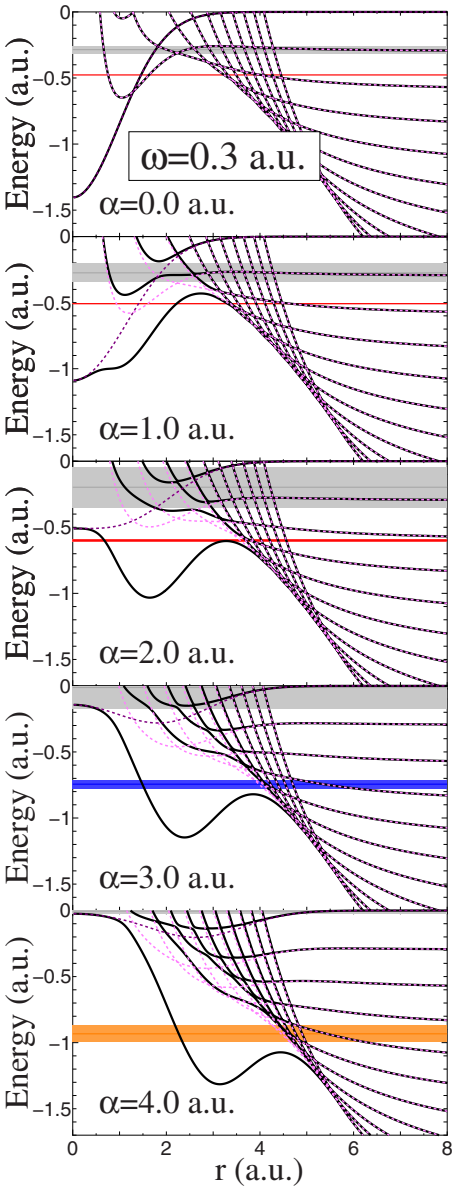

FIG. 3. (Color online) The adiabatic potential curves (black solid curves) and the diabatic potential curves (pink and purple dashed curves) for $\mu=0$. The purple dashed curve represents the KH potential. The laser angular frequency is fixed to $\omega=0.3$. The values of the ponderomotive radius α are shown in each figure. The horizontal bands indicate the positions and widths of the resonances corresponding to the dominant poles of the same color in Fig. 1(a).

curves are enhanced and push down the lowest potential curve so as to form a well. With increasing α, the position of the maximum shifts toward large r, and the potential well is also shifted in the same direction.

On the basis of the change in the shape of the lowest adiabatic curve, a physical picture of ionization is obtained as follows: when $0<\alpha\leq 2.0$, ionization is ascribable to the tunneling through the potential barrier. When $\alpha\geq 2.0$, the resonance energy level is lifted above the top of the barrier, and the BSI takes place. This intuitive picture is verified by the calculation of the single channel scattering, in which only the lowest adiabatic potential is taken into account. Complex

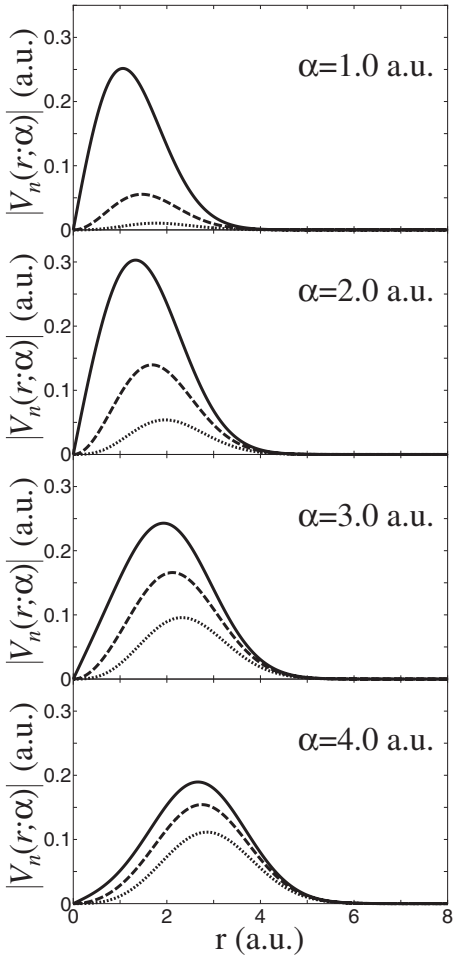

FIG. 4. The absolute values of the off-diagonal elements of the effective potential matrix as a function of r. The values $|V_1(r;\alpha)|$, $|V_2(r;\alpha)|$, and $|V_3(r;\alpha)|$ are shown by the solid, dashed, and doted curves, respectively.

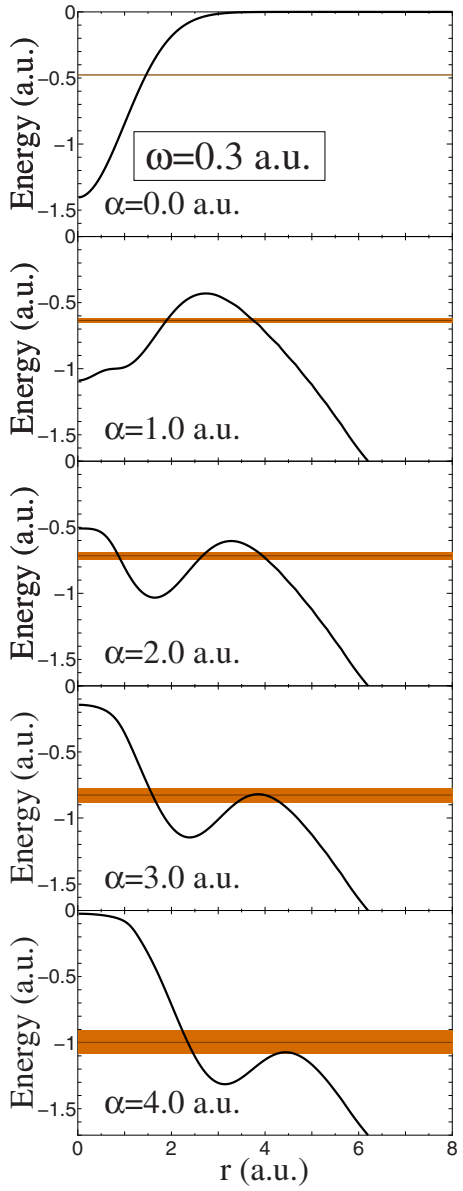

FIG. 5. (Color online) The position and width of the resonance formed in the single-channel scattering on the lowest adiabatic potential curve for the value of α indicated in the figure. The laser angular frequency is fixed to $\omega=0.3$. The (brown) horizontal bands indicate the positions and widths of the resonances. In the case of $\alpha=0.0$, the horizontal line indicates the position of the bound state.

energy eigenvalues were calculated on the basis of the complex absorbing potential (CAP) method [30,31], and the position and width of the shape resonance were obtained. The details of the calculation are described in Appendix C. The results are shown in Fig. 5. The resonance position and width approximately agree with exact ones shown in Fig. 3, respectively. In conclusion, the tunneling ionization and the BSI can be interpreted as decay of the shape resonance formed on the lowest adiabatic potential of the Floquet formalism.

B. High-frequency regime

The potential curves for the high-frequency regime $\omega=0.6$ are shown in Fig. 6. The lowest adiabatic potential possesses a shallow well when $\alpha=1.0$. For $\alpha\geq 2.0$, however, no potential well is formed. In comparison with the case of $\omega=0.3$, the larger channel interval makes the envelope of the diabatic curves more steep. As a result, the lowest adiabatic potential curve is too steep to form a well even in the presence of the localized level repulsions. It should be noted that the off-diagonal elements are independent of ω. The difference in the shape of the lowest adiabatic curve is solely ascribed to the difference in the interval of the Floquet channels.

In this regime, the original bound state shifts upward as α increases and becomes a resonance trapped, roughly speaking, in the well of the diabatic potential $[V_{\mathrm{eff}}^{\mu=0}(r;\alpha)]_{00}$, i.e., the KH potential. The wave function of the resonance state leaks through the potential crossings. In the cases of $\alpha=1.0$ and 2.0, the KH potential undergoes potential crossings with large energy gaps as shown in Fig. 6. As a result, the resonance width becomes very large. When $\alpha\geq 2.0$, the energy gaps of the avoided crossings decrease with increasing α, indicating that the KH high-frequency approximation becomes better, and the stabilization occurs. This is none other

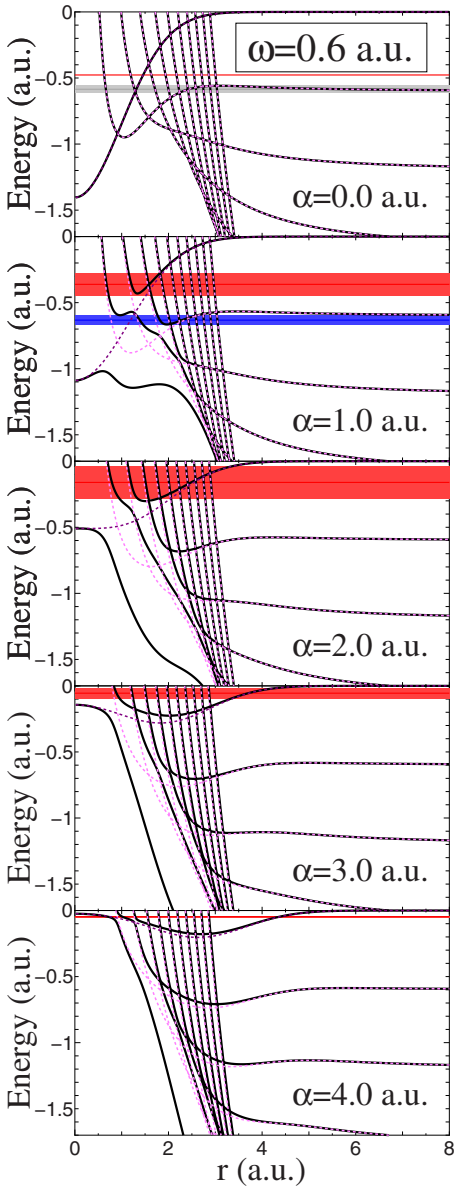

FIG. 6. (Color online) The same as Fig. 3, except that the angular frequency is $\omega=0.6$.

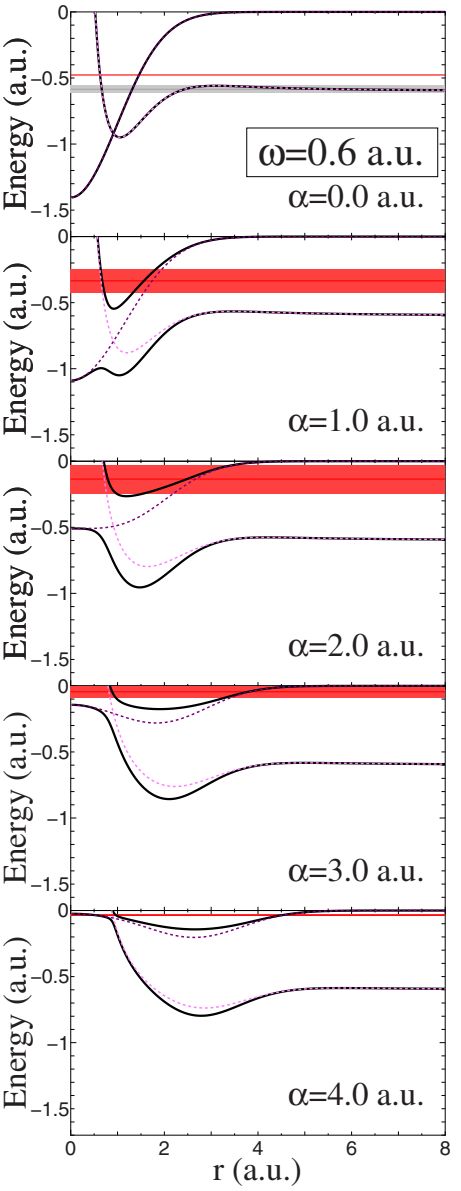

FIG. 7. (Color online) The results of the two channel model including only the Floquet channels $n=-1$ and 0. The meanings of the solid and dashed curves are the same as Fig. 6.

than the KH stabilization discussed by Popov *et al.* [24]. The reduction in the energy gaps is ascribable to the shift of the peak of the off-diagonal matrix elements $V_{n\neq 0}(r;\alpha)$ as a function of r. With increasing α, the peak position of $|V_{n\neq 0}(r;\alpha)|$ shifts toward large r as shown in Fig. 4, and consequently, the avoided crossings occurring at the region of the potential well become small. It should be noted that the avoided crossings caused by the Floquet channels of $|n|>10$, which were neglected in Figs. 3 and 6, should have smaller energy gaps.

The stabilization of the resonance originating from the bound state can be explained by considering two Floquet channels as follows: the calculation of the S-matrix pole position was carried out by considering only two Floquet channels, $n=0$ and -1. The resonance position and width obtained for several values of α are shown in Fig. 7 together with the adiabatic and the diabatic curves also obtained by the two-channel model. The resonance position and width approximately agree with the exact ones in Fig. 6. Thus, the resonance state in question can be interpreted as the Feshbach resonance, in which the quasibound state on the KH potential decays into the Floquet channel $n=-1$.

On the other hand, the fate of the shape resonance discussed in Sec. III C can also be explained by the potential curves in Fig. 6. As α increases, the shape resonance begins to shift downward and crosses the channel threshold. As discussed in Sec. III C, the role of the dominant pole seems to be succeeded by another pole, and the resonance continues to exist for a while. When $\alpha=2.0$, however, no potential well is formed in the lower energy region, and the resonance disappears. It should be noted that the resonance in question is not reproduced in the two-channel model for $\alpha\geq 1.0$ as can be seen in Fig. 7.

V. DISCUSSION

A. Transition between low- and high-frequency regimes

As discussed so far, the tunneling ionization with a smooth ponderomotive energy shift typically occurs in the low-frequency regime, while the KH stabilization is observed in the high-frequency regime. Transition between the low- and the high-frequency regimes can be viewed as follows: the tunneling ionization can be ascribable to the decay of resonance state formed in the lowest adiabatic potential. When ω increases and approaches to the one-photon ionization threshold ω_b, the potential well becomes shallow, and consequently, the resonance is formed only for small α. The ponderomotive energy shift is quitted at a certain value of α as shown in Fig. 1(b). The picture of the tunneling ionization or the BSI becomes invalid beyond that value of α. Thus, the tunneling ionization accompanied by the ponderomotive energy shift can be observed only when the laser frequency is sufficiently lower than the one-photon ionization threshold.

On the other hand, it should be noted that the KH stabilization, which has been discussed as the typical phenomenon in the high-frequency regime, is observed also in the low-frequency regime. As mentioned in Sec. III A, the shape resonance exhibits the stabilization as can be seen in Figs. 1(a) and 1(b). From an inspection of the adiabatic potential curves for $\omega=0.3$ shown in Fig. 3, it is inferred that a kind of KH stabilization occurs. In the case of $\alpha=4.0$, for instance, a shallow potential well can be seen in the region of $-0.1 \leq E < 0$ if one traces the potential curve diabatically. Although the potential well undergoes several avoided crossings, the energy gaps are small. If α increases beyond 4.0, the energy gaps are expected to become smaller, and the diabatic representation also becomes better. The resonance trapped in the diabatic well is expected to have a long lifetime. This mechanism is interpretable as a kind of KH stabilization.

The stabilization of the shape resonance observed in the case of $\omega=0.5$ is also proven to be the KH stabilization by an inspection of the adiabatic potential curves. The stabilization observed in the case of $\omega=0.6$ is a typical KH stabilization as discussed in Sec. IV B. Accordingly, the KH stabilization, including that of the generalized sense discussed above, is observed in all of four cases shown in Fig. 1. The difference between the low- and high-frequency regimes is in the origin of resonances. In the cases of $\omega=0.3$, 0.4, and 0.5, the resonance exhibiting the KH stabilization originates from the shape resonance in the null field. In the case of $\omega=0.6$, however, it is the resonance originating from the bound state that exhibits the KH stabilization.

The transition between the low- and high-frequency regimes can be summarized as follows: when ω is sufficiently smaller than ω_b, ionization of the atom originally in the bound state is ascribable to the tunneling ionization. On the other hand, the shape resonance state exhibits the KH stabilization of the generalized sense. When the value of ω is in the vicinity of ω_b, the picture of tunneling ionization breaks down. The mechanism of the ionization has to be ascribed to a result of complicated mutichannel scattering. However, the KH stabilization of the shape resonance remains to occur. When ω further increases and exceeds a certain critical value ω_c, the bound state of the atom exhibits the KH stabilization. In this regime, the behavior of the shape resonance cannot be explained by a simple picture.

The critical value ω_c dividing the low- and high-frequency regimes falls between 0.5 and 0.6 in the present model. It can intuitively be understood that the inequality $\omega_c > \omega_b$ holds because of the following reason. The shape resonance in question is always in the Floquet block of $n=-1$, while the bound state is in the block of $n \leq -2$ when $\omega < \omega_b$. This means that the energy position of the shape resonance is higher than that of the bound state. If the system changes adiabatically with increasing α, the lower state, i.e., the bound state, exhibits a downward shift interpretable as the ponderomotive energy shift. The upper state, i.e., the shape resonance, shifts upward and will be trapped in the KH potential.

The behaviors of the pole trajectories in the case of $\omega=0.5$ shown in Fig. 1(c), however, imply that prediction of the precise value of ω_c by an intuitive argument is difficult. In this case, the bound state is the upper state. However, the bound state shifts downward, and the shape resonance exhibits an upward shift and the KH stabilization. The two trajectories, as can clearly be seen in the inset of Fig. 1(c), undergo a kind of avoided crossing on the complex energy plane. Such collision of resonance poles implies that two resonance states are interacting with each other [13]. In such a situation, it is difficult to predict the motions of trajectories intuitively on the complex energy plane. When ω was increased to 0.6, it seems that the energy difference became sufficiently large so as make the upper state shift upward. Thus, it is inferred that the value of ω_c depends very delicately on the relative position of the bound state and the shape resonance on the complex energy plane. According to the discussion so far, it can be stated at most that ω_c falls in the vicinity of $\omega_b + E_{res}$, where E_{res} is the energy of the shape resonance in the null field.

B. Tunneling ionization and BSI in the framework of the Floquet formalism

The intuitive picture of the tunneling ionization and BSI is usually based on the equations of motion in the length gauge, in which electrons are driven solely by electrostatic fields. The theory derived along this line is the ADK theory [5]. In the length gauge, however, the interaction between the electrons and the laser field extends to the asymptotic region $r \to \infty$. Consequently, the scattering theory is not applicable to the ionization processes if the length gauge is employed. One has to choose the acceleration gauge for the scattering theoretical treatment. The scattering theoretical description of ionization, based on the Floquet formalism in the acceleration gauge, has been known to be suitable for the high-frequency regime [23,26]. It seems to be disadvantageous, at first sight, to apply the Floquet formalism to the low-frequency regime. The results in Sec. IV A, particularly in Figs. 3 and 4, however, indicate that the Floquet formalism successfully provides an intuitive picture. The ionization in the low-frequency regime can again be understood as the

tunneling through the potential barrier defined in the Floquet formalism with the acceleration gauge. It should be noted that the picture of tunneling within the Floquet formalism remains valid for higher-frequency region in the low-frequency regime as discussed below.

The conventional criterion for the validity of the tunneling mechanism is given by the Keldysh parameter $\gamma = \sqrt{I_p/(2U_p)}$, where I_p is the ionization energy of an atom and $U_p = \omega^2\alpha^2/4$ is the ponderomotive energy [2]. When $\gamma < 1$, the atomic ionization is believed to take place by the tunneling mechanism. As regard to the present model in the low-frequency regime, the Keldysh parameter is estimated as $\gamma = 3.26/\alpha$ with the fixed value of $\omega = 0.3$. According to the conventional criterion, the tunneling ionization could be observed only for $\alpha > 3.26$. Therefore, the behavior of the pole trajectory, i.e., a smooth connection of trajectories reproducing the ponderomotive energy shift, observed in Fig. 1(a) cannot be explained by the tunneling ionization in the usual sense. As discussed in Sec. IV A, however, the behavior of the pole trajectory can clearly be explained by a single adiabatic potential with a barrier even in the case of $\alpha < 3$ as shown in Fig. 5. This implies that the picture of tunneling remains valid in the Floquet formalism even when $\gamma > 1$. Under the same condition, needless to say, the ADK theory does not work well. The argument so far suggests that the Floquet formalism in the acceleration gauge provides the picture of tunneling ionization in a sense slightly different from that of the ADK theory. In the limit of small γ, two pictures of tunneling should coincide with each other. It is emphasized again that the picture of tunneling in the Floquet formalism remains valid for higher laser frequencies than that predicted by the conventional criterion based on the Keldysh parameter.

As discussed so far, the behaviors of the resonances, i.e., the dominant poles, are clearly explicable by the adiabatic potentials. As regard to the motions of the shadow poles, however, there is no explanation at hand. As can be seen in Fig. 1, the behaviors of poles as a whole could be understood much more clearly if one had a certain intuition concerning the motions of shadow poles. This point is left for future studies.

C. Advantage of the two-dimensional model

As discussed in Secs. IV and V A, the transition between the low- and high-frequency regimes is successfully explained by the change in the shape of the adiabatic potential curves due to avoided crossings. It should be noted that no avoided crossing occurs in the 1D model due to the lack of the centrifugal potential. In the 1D Floquet model, all the diabatic curves are generated by shifting one original potential curve. As a result, the infinite numbers of curves having the same shape run parallel with each other for any value of α. Therefore, no avoided crossing occurs in the adiabatic curves. The discussion of the ionization mechanisms like that in Sec. IV is not possible in the 1D model, although there is similarity between the 1D and 2D models with respect to the behaviors of the *S*-matrix pole trajectories, particularly in the high-frequency regime as shown in Figs. 1(d) and 2.

The ionization mechanism of one-electron 3D atom, e.g., the realistic H atom, in intense laser fields could be elucidated in the manner similar to the 2D model. There is similarity between the 2D and 3D treatments in that the centrifugal potential exists in both the cases. In the 3D treatments, the diabatic channels should be labeled by three quantum numbers: the index of the Floquet block n_F, the azimuthal quantum number l, and the magnetic quantum number m. In the case of circularly polarized laser field with the polarization vector rotating perpendicularly to the axis of quantization, a new quantum number $\mu = m - n_F$ remains good as in the 2D case due to the rotational symmetry of the light-atom system. Linked up with the periodicity with respect to the quasienergy, the quasieigenstates with different μ are replicas of one identical state, e.g., that with $\mu = 0$, as discussed below Eq. (14). The 2D model in the present study can be interpreted as a model in which the physics is simplified by neglecting the degree of freedom corresponding to l. In this respect, the cost of numerical calculation is reduced in the present 2D model in comparison with the 3D treatment. On the other hand, the selection rule of coupling is changed in the case of the linearly polarized light. The axis of quantization being chosen as parallel to the polarization vector, the magnetic quantum number m is good in this case. It suffices to solve the close-coupling equations for each m. Unlike the quantum number μ discussed above, m is not linked with the periodicity of the quasienergy, and one has to solve the coupled equations for different m's. By reduction to the 2D model, one merely loses the good quantum number m, and the cost of calculation is not much reduced.

The discussion of the ionization mechanism based on the diabatic and adiabatic curves could be applied to two-electron atoms, such as He and H^-, by the use of the hyperspherical coordinate [32]. When the hyper-radius of the two-electron system is treated as the scattering coordinate, one can construct, in a manner analogous to that in Sec. IV, the adiabatic potential curves which describe the ionization processes. The adiabatic curves are expected to exhibit avoided crossings due to not only the coupling with the laser field but also the electron correlation. The effects of the electron repulsion exerted on the ionization processes would come into the scope of investigations.

VI. CONCLUSION

On the basis of the Floquet formalism, the 2D model atom in circularly polarized intense laser fields is analyzed. The *S*-matrix pole trajectories on the complex quasienergy Riemann surface are calculated. In the low-frequency regime, the tunneling ionization accompanied with the ponderomotive energy shift is typically observed. On the other hand, the stabilization phenomenon is observed in the high-frequency regime. In order to obtain a unified view, a particular attention is focused on the adiabatic potential curves for the radial motion of the electron in the acceleration gauge. The tunneling ionization can be explained again by the tunneling through the lowest adiabatic potential. The ponderomotive energy shift and the ionization rate can be reproduced by the single channel scattering on the lowest adiabatic potential.

On the other hand, the stabilization in the high-frequency regime can be explained by the scattering in which two diabatic channels are involved. The transition between the low- and high-frequency regimes can be elucidated by the change in the shape of the adiabatic potential curves due to avoided crossings.

APPENDIX A: COMPUTATIONAL METHOD OF THE HANKEL FUNCTION FOR THE COMPLEX VARIABLE

The value of $H_{n+\mu}^{(+)}(z)$ for the complex variable $z=k_n r$ is required in the Siegert boundary condition [Eq. (17)]. The numerical values can be obtained by using the following formulas [35]:

$$H_\nu^{(+)}(z) = \sqrt{\frac{2}{\pi z}} \frac{\exp[i(z-\pi\nu/2-\pi/4)]}{\Gamma(\nu+1/2)} \times \int_0^\infty \left(1+\frac{it}{2z}\right)^{\nu-1/2} t^{\nu-1/2} e^{-t} dt \left[-\frac{\pi}{2} < \arg z < \frac{3\pi}{2} \text{ and } \nu \geq 0 \right], \tag{A1}$$

$$H_{-\nu}^{(+)}(z) = (-1)^\nu H_\nu^{(+)}, \tag{A2}$$

$$H_\nu^{(+)}(z) = (-1)^{\nu m} H_\nu^{(+)}(e^{m\pi i} z) + 2m J_\nu(z). \tag{A3}$$

Here, $J_\nu(z)$ represents the Bessel function for any integer value $\nu=n+\mu$.

For the dominant poles, the value of $H_{n+\mu}^{(+)}(z)$ is given by the principal value with z in the range $-\pi < \arg z \leq \pi$. When the dominant pole becomes a shadow pole by crossing the negative real axis of z, the analytic continuation is required, and the value of $H_{n+\mu}^{(+)}(z)$ should be calculated by using formula (A3), in which the integer value m specifies the Riemann sheet of the complex z plane.

APPENDIX B: METHOD OF SOLVING THE CLOSE-COUPLING EQUATIONS [EQ. (15)]

The process of calculation is started by integrating Eq. (15) for a trial value of E. A set of N linearly independent column vectors of the radial functions, $\{\boldsymbol{g}_1, \boldsymbol{g}_2, \ldots, \boldsymbol{g}_N\}$, is prepared so as to satisfy the Siegert boundary condition [Eq. (17)], with a set of the N signs, Σ. In addition, another set, $\{\boldsymbol{g}_1', \boldsymbol{g}_2', \ldots, \boldsymbol{g}_N'\}$, is prepared so as to satisfy the boundary condition of Eq. (17) with $H_{n+\mu}^{(+)}(k_n r)$ replaced by the derivative $dH_{n+\mu}^{(+)}(k_n r)/dr$. The propagation of these two sets is carried out by the Runge-Kutta method from the asymptotic region to a matching point, and $N \times N$ matrices $\boldsymbol{G}_r^\mu = (\boldsymbol{g}_1, \boldsymbol{g}_2, \ldots, \boldsymbol{g}_N)$ and $\boldsymbol{G}_r^{\mu'} = (\boldsymbol{g}_1', \boldsymbol{g}_2', \ldots, \boldsymbol{g}_N')$ are obtained. A similar calculation is carried out outward to the same matching point from a vicinity of the origin with the boundary condition [Eq. (18)] as well as its derivative, and $N \times N$ matrices $\boldsymbol{G}_l^\mu$ and $\boldsymbol{G}_l^{\mu'}$ are obtained. At the matching point the continuity of the wave function and its derivative requires

$$\boldsymbol{G}_l^\mu \boldsymbol{L} = \boldsymbol{G}_r^\mu \boldsymbol{R} \tag{B1}$$

and

$$\boldsymbol{G}_l^{\mu'} \boldsymbol{L} = \boldsymbol{G}_r^{\mu'} \boldsymbol{R}, \tag{B2}$$

where $\boldsymbol{L}$ and $\boldsymbol{R}$ are certain unknown column vectors with N components. The two matching conditions [Eqs. (B1) and (B2)] can be combined as (e.g., see [33,34])

$$\begin{pmatrix} \boldsymbol{G}_l^\mu & \boldsymbol{G}_r^\mu \\ \boldsymbol{G}_l^{\mu'} & \boldsymbol{G}_r^{\mu'} \end{pmatrix} \begin{pmatrix} \boldsymbol{L} \\ -\boldsymbol{R} \end{pmatrix} = \boldsymbol{0}. \tag{B3}$$

Therefore, the matching condition requires that the determinant of the matrix in Eq. (B3) vanishes, i.e.,

$$D(E) = \det \begin{pmatrix} \boldsymbol{G}_l^\mu & \boldsymbol{G}_r^\mu \\ \boldsymbol{G}_l^{\mu'} & \boldsymbol{G}_r^{\mu'} \end{pmatrix} = 0. \tag{B4}$$

The solution is obtained by the Newton-Raphson method, and the complex quasienergies E are determined.

APPENDIX C: THE CAP METHOD

The complex energy eigenvalues of the lowest adiabatic potential for the laser angular frequency $\omega=0.3$ are calculated by using the CAP method [30,31] as follows: the radial function $-i\eta r^6$ is added to the lowest adiabatic potential $V_{\text{ad}}(r;\alpha)$. An artificial Hamiltonian is defined as

$$H(\eta) = -\frac{1}{2r}\frac{d}{dr}\left(r\frac{d}{dr}\right) + V_{\text{ad}}(r;\alpha) - i\eta r^6. \tag{C1}$$

The complex energy eigenvalues $E(\eta)$ are calculated by diagonalizing the Hamiltonian matrix constructed by using the discrete variable representation [36]. The mesh point of r is $r_j=(j-1/2)\Delta r$, where $\Delta r=0.05$ and $j=1,2,\ldots,400$, and the numerical data of the lowest adiabatic potential $V_{\text{ad}}(r;\alpha)$ at each mesh point are prepared by diagonalizing the effective potential matrix [Eq. (16)] including the Floquet channels $n=-60,-59,\ldots,5$. The optimal values of η are determined from the condition [30,31]

$$\left| \eta \frac{dE(\eta)}{d\eta} \right| = \min \tag{C2}$$

and the values of $\eta=1.40\times10^{-7}$, 1.30×10^{-7}, 1.50×10^{-7}, and 1.45×10^{-7} are used for the cases of $\alpha=1.0$, 2.0, 3.0, and 4.0, respectively.

[1] K. Yamanouchi, Science **295**, 1659 (2002).
[2] L. V. Keldysh, Zh. Eksp. Teor. Fiz. **47**, 1945 (1964) [Sov. Phys. JETP **20**, 1307 (1965)].
[3] F. H. M. Faisal, J. Phys. B **6**, L89 (1973).
[4] H. R. Reiss, Phys. Rev. A **22**, 1786 (1980).
[5] M. V. Ammosov, N. B. Delone, and V. P. Krainov, Zh. Eksp. Teor. Fiz. **91**, 2008 (1986) [Sov. Phys. JETP **64**, 1191 (1986)].
[6] M. Pont and M. Gavrila, Phys. Rev. Lett. **65**, 2362 (1990).
[7] J. N. Bardsley, A. Szöke, and M. J. Comella, J. Phys. B **21**, 3899 (1988).
[8] R. M. Potvliege, Phys. Scr. **68**, C18 (2003).
[9] J. C. Wells, I. Simbotin, and M. Gavrila, Phys. Rev. Lett. **80**, 3479 (1998).
[10] M. Dörr and R. M. Potvliege, Phys. Rev. A **41**, 1472 (1990).
[11] G. Yao and Shih-I Chu, Phys. Rev. A **45**, 6735 (1992).
[12] M. Marinescu and M. Gavrila, Phys. Rev. A **53**, 2513 (1996).
[13] T. Yasuike and K. Someda, Phys. Rev. A **66**, 053410 (2002).
[14] A. S. Fearnside, R. M. Potvliege, and R. Shakeshaft, Phys. Rev. A **51**, 1471 (1995).
[15] T. Yasuike and K. Someda, Phys. Rev. A **71**, 017402 (2005).
[16] R. M. Potvliege and P. H. G. Smith, Phys. Rev. A **48**, R46 (1993).
[17] P. Marte and P. Zoller, Phys. Rev. A **43**, 1512 (1991).
[18] M. Dörr, P. G. Burke, C. J. Joachain, C. J. Noble, J. Purvis, and M. Terao-Dunseath, J. Phys. B **26**, L275 (1993).
[19] L. Dimou and F. H. M. Faisal, Phys. Rev. A **46**, 4442 (1992).
[20] L. Dimou and F. H. M. Faisal, Phys. Rev. A **49**, 4564 (1994).
[21] H. G. Muller and M. Gavrila, Phys. Rev. Lett. **71**, 1693 (1993).
[22] N. J. van Druten, R. C. Constantinescu, J. M. Schins, H. Nieuwenhuize, and H. G. Muller, Phys. Rev. A **55**, 622 (1997).
[23] M. Gavrila, J. Phys. B **35**, R147 (2002).
[24] A. M. Popov, O. V. Tikhonova, and E. A. Volkova, J. Phys. B **36**, R125 (2003).
[25] M. Dörr, R. M. Potvliege, D. Proulx, and R. Shakeshaft, Phys. Rev. A **43**, 3729 (1991).
[26] M. Gavrila, in *Atoms in Intense Laser Fields*, edited by M. Gavrila (Academic Press, New York, 1992), p. 435.
[27] Shih-I Chu, Adv. At. Mol. Phys. **21**, 197 (1985).
[28] R. M. Potvliege and R. Shakeshaft, Phys. Rev. A **38**, 6190 (1988).
[29] J. R. Taylor, *Scattering Theory* (Wiley, New York, 1972).
[30] U. V. Riss and H.-D. Meyer, J. Phys. B **26**, 4503 (1993).
[31] S. Sahoo and Y. K. Ho, J. Phys. B **33**, 2195 (2000).
[32] C. D. Lin, Phys. Rep. **257**, 1 (1995).
[33] R. G. Gordon, J. Chem. Phys. **51**, 14 (1969).
[34] B. R. Johnson, J. Chem. Phys. **69**, 4678 (1978).
[35] I. S. Gradshteyn and I. M. Ryzhik, *Table of Integrals, Series, and Products* (Academic Press, New York, 1980), Chap. 8.
[36] A. G. Borisov, J. Chem. Phys. **114**, 7770 (2001).